Biomass Conversion and Biorefinery (2023) 13:3819–3836
https://doi.org/10.1007/s13399-021-01384-2

ORIGINAL ARTICLE

Comparison between two Eulerian-Lagrangian methods: CFD-DEM and MPPIC on the biomass gasification in a fluidized bed

Chunlei Li[1] · Qitai Eri[1]

Received: 14 December 2020 / Revised: 1 February 2021 / Accepted: 15 February 2021 / Published online: 25 February 2021

Abstract

This paper compares the two Eulerian-Lagrangian methods, computational fluid dynamics–discrete element method (CFD-DEM) and multiphase particle-in-cell (MPPIC), in simulating the biomass gasification in the fluidized bed. A series of reactions, including the drying, pyrolysis, and homogeneous and heterogeneous reactions, are implemented. The composition of the product gases is predicted and the trajectories, diameters, heat transfers, and temperatures of the discrete particles are compared. The effects of steam-to-biomass ratio and reactor temperature are explored. The results show that the difference between the MPPIC and the CFD-DEM in predicting the H_2 share is no more than 0.26%, while the errors between the simulation and the experiment are 0.45% (CFD-DEM) and 0.71% (MPPIC), respectively. Besides, both the CFD-DEM and MPPIC show the same trend when changing the operating parameters. Therefore, we think, although there are discrepancies between MPPIC and DEM in particle-scale details, for the reactor-scale applications, e.g., predicting the composition of the product gas, the MPPIC is adequately accurate as DEM.

Keywords Biomass gasification · Fluidized bed · Eulerian-Lagrangian · CFD-DEM · MPPIC · MFiX

1 Introduction

Biomass gasification is a promising technology to produce renewable energy through thermochemical conversion. One advantage of this technology is that it produces clean product, i.e., the mixture of CO and H_2 (also known as syngas) or H_2 alone. The syngas not only is useful in the Fisher-Tropsch process but also can serve as a fuel directly [1]. However, the prediction of the gasification products is complex and challenging due to the complexity of biomass composition and gasification reactions [1, 2].

Many methods are developed to study the gasification process in the fluidized bed, including the experimental methods [3] and the simulation methods [4]. Among them, computational fluid dynamics (CFD) is one of the ways that are inexpensive, safe, and capable of attaining the details of the process, comparing to the experimental methods [1, 4, 5]. Currently, two common CFD methods are widely used to simulate the gasification in the fluidized bed: the Eulerian-Eulerian method (EE) and the Eulerian-Lagrangian method (EL). Many comparative studies between these two methods have been reported [6–10]. The Eulerian-Eulerian method has edges in simulating the large-scale fluidized bed with relatively low computational cost, but it omits lots of details of the particles. On the contrary, whereas the Eulerian-Lagrangian method is costly in computing resources, it gives details about particles. Thus, with the increase of computing power, more and more researches on utilizing the Eulerian-Lagrangian method in simulating gasification in a fluidized bed emerge [11–19].

Today, two Eulerian-Lagrangian methods gain the most focuses: one is the CFD–discrete element method (DEM) [20]; the other is the multiphase particle-in-cell (MPPIC) [21]. Both of them are the Eulerian-Lagrangian method, which means they are capable of constructing particle-scale models. That is, the solid surface reactions, core shrinking, and particle tracking, etc. are possible for these two methods.

However, the difference between CFD-DEM and MPPIC also exists [22]. The main difference is that the MPPIC calculates the particle motion on the scale of cells instead of discrete

✉ Qitai Eri
eriqitai@buaa.edu.cn

[1] School of Energy and Power Engineering, Beihang University, Beijing 100191, China

particles. It first lumps the particles in cells, then calculates the position of the particles by the Liouville equation on the cell scale, and finally distributes the particles' attributes, e.g., locations, velocities, and diameters back to the particles. That is also why it is called the particle-in-cell method [23].

The DEM treats the particle as the elastic balls and treats the collision behavior as the collision between two or more elastic balls [20]. This is the so-called soft-sphere model in DEM [24]. On the other hand, the MPPIC does not resolve the collision process itself, which substantially enlarges the solid time step and boosts the simulation. Instead, it treats the collision as a probability event: the denser the solid phase is, the higher likelihood the particles may collide [21]. Besides, the colliding force is not calculated by elastic deformation as the DEM does. Rather, it is given by the solid stress term [25]. These treatments substantially decrease the computational expense of MPPIC, but it inevitably sacrifices the accuracy of the hydrodynamical prediction of particles.

Another key feature of MPPIC is the use of "parcel." This method packages a number of particles (usually tens of particles) into a group, which substantially reduces the number of actually calculated particles. However, such a technique is not exclusive to the MPPIC. In fact, recent studies also utilized the parcel concept in CFD-DEM, like [26–28]. They are usually called coarse-grained CFD-DEM, but the concept of "parcel" is the same as MPPIC. Therefore, in this work, we keep the parcel weight (the number of particles in a parcel) as one to eliminate the difference related to "parcel."

In fact, the computation efficiency of MPPIC is usually much higher than the DEM, especially when the number of particles is large. Due to the neighbor searching algorithm adopted by the DEM to search the colliding objects, the time complexity of DEM is growing with the square of particle numbers [29, 30]. In contrast, the MPPIC is less sensitive to the particle numbers since it does not use the neighbor searching algorithm. This limits the application of the DEM in large-scale simulation, especially the 3D simulation. Besides, although the MPPIC is less accurate in particle-scale hydrodynamics, it is not certain that whether this inaccuracy will cause a large error in reactive flow, whose error is also affected by the heat transfer and the reactions. Therefore, the discrepancy between the MPPIC and the DEM on simulating reactive flow is not clear yet.

Although so far, several studies have reported the difference of the two Lagrangian methods in predicting the hydrodynamics [9, 10, 22, 31], there is little piece of literature to evaluate the two methods simulating the reactive flow, especially the biomass gasification. Instead, most of these documented studies focus on the cold flow. However, the reactive flow is greatly affected by the chemical reactions; thus, those studies are probably not suitable in evaluating the accuracy of the model to predict gasification production. Therefore, it is necessary to conduct a study to compare the two methods, which focuses on the reactions and gasification results rather than the hydrodynamics of the fluidized bed.

The novelty of this work can be stated as below:

- A comparison of the CFD-DEM and MPPIC, focusing on the gasification rather than the hydrodynamics, is made.
- A comprehensive, full-detailed description of the fluidized bed, from the reactor-scale to the particle-scale, is made, which includes:

  – Time consumption of the serial runs and parallel runs (16 threads).
  – Hydrodynamics: trajectories, instant particle distributions, the evolution of pressure drop, the time-averaged field of pressure and volume fraction, etc.
  – Thermodynamics: transient details of the heat transfer on the particles, the evolution of heat transfer, the heat transfer from different mechanisms (conduction, convection, radiation, the heat of reactions, etc.), the evolution of gas temperature, etc.
  – Chemical reactions: molar fraction contour of the CO, H2, the composition of product gas, etc.
  – Particle-scale details: the evolution of temperature of particles, heat transfer on the selected particles, the evolution of the solid species mass fractions, the shrinkage of the particles, Reynolds number of the particles, etc.

This paper aims to compare the CFD-DEM and the MPPIC, to attain the difference between the two methods, and to examine whether it is reasonable to replace the DEM with MPPIC in a fluidized bed biomass gasification simulation. The results of the experiment will serve as a reference. Hydrodynamical, thermodynamical, and reaction-related details of the field and the particles will be discussed in the comparison. The composition of four product gases (CO, CO_2, CH_4, H_2) will be predicted. Besides, the effects of the steam-to-biomass ratio (SBR) and the reactor temperature will be respectively explored to comprehensively evaluate the discrepancies of the two methods under various circumstances.

2 Mathematical modeling

2.1 Governing equations of hydrodynamics

2.1.1 Fluid phase equations

The continuity equation of the fluid phase is

$$\frac{\partial\left(\varepsilon_g\rho_g\right)}{\partial t}+\nabla\cdot\left(\varepsilon_g\rho_g\boldsymbol{u}_g\right)=\delta\,\dot{m}_p \tag{1}$$

Table 1 Chemical reactions [43, 44]

ID	Reactions	Reaction rate
R0: drying	$H_2O(L) \rightarrow H_2O(G)$	$r_0 = 5.12 \times 10^{10} \exp\left(\frac{-10585}{T_p}\right) m_{moi}/MW_{moi}$
R1: pyrolysis	$C_{19.32}H_{27.57}O_{12.03} \rightarrow 11.37CO + 0.33CO_2 + 3.213\ CH_4 + 7.36H_2 + 4.41C$	$r_1 = 5 \times 10^6 \exp\left(\frac{-1.28\times10^8}{8314T_p}\right) m_{vol}/MW_{vol}$
R2: Boudouard [45]	$C + CO_2 \rightarrow 2CO$	$r_{kin} = 0.3\ T_p \exp\left(\frac{-2\times10^8}{8314\times T_p}\right)$ $r_{diff} = 5 \times 10^{-12} \left(\frac{T_g+T_p}{2}\right)^{0.75}/D_p$ $r = \frac{1}{MW_C} A_p\ p_{CO2} r_{diff}\ \frac{r_{kin}}{r_{diff}+r_{kin}}$
R3: steam reforming[45]	$C + H_2O \rightarrow CO + H_2$	$r_{kin} = 2T_p \exp\left(\frac{-1.96\times10^8}{8314\times T_p}\right)$ $r_{diff} = 5 \times 10^{-12} \left(\frac{T_g+T_p}{2}\right)^{0.75}/D_p$ $r = \frac{1}{MW_C} A_p\ p_{H_2O} r_{diff}\ \frac{r_{kin}}{r_{diff}+r_{kin}}$
R4: methane gasification	$CH_4 + H_2O \rightarrow CO + 3\ H_2$	$r = 3 \times 10^8 \exp\left(\frac{-1.26\times10^8}{8314\times T_g}\right) [CH_4]\ [H_2O]$
R5: water-gas shift[46]	$CO + H_2O \leftrightarrow CO_2 + H_2$	$r_f = 2.78 \times 10^3 \exp\left(\frac{-1.26\times10^7}{8314\times T_g}\right) [CO]\ [H_2O]\ r_b = 9.59 \times 10^4 \exp\left(\frac{-4.66\times10^7}{8314\times T_g}\right) [H_2]\ [CO_2]\ k_{eq} = 0.029\exp\left(\frac{3.4\times10^7}{8314\times T_g}\right), r = r_f - r_b/k_{eq}$

The momentum equation of the fluid phase is

$$\frac{\partial\left(\varepsilon_g \rho_g \boldsymbol{u_g}\right)}{\partial t} + \nabla \cdot \left(\varepsilon_g \rho_g \boldsymbol{u_g} \boldsymbol{u_g}\right) = \nabla \cdot \left(\varepsilon_g \boldsymbol{\tau_g}\right) - \nabla p + \varepsilon_g \rho_g g - \sum_{m=1}^{M} I_{gm} \tag{2}$$

where the viscous stress tensor is

$$\tau_{gij} = \mu_g \left(\frac{\partial u_{gi}}{\partial x_j} + \frac{\partial u_{gj}}{\partial x_i}\right) - \frac{2}{3} \mu_g \frac{\partial u_{gk}}{\partial u_{gk}} \delta_{ij} \tag{3}$$

The I_{gm} is the momentum exchange term between the gas and the mth phase solid (i.e., sand or biomass). δ_{ij} is the Kronecker delta.

Further details about the gas phase hydrodynamic governing equations can refer to [29, 32–35]

2.1.2 Particle motion

In the Lagrangian method, particle motion is controlled by Newton's 2nd law, i.e.,

$$m_p \frac{d\boldsymbol{u_p}}{dt} = \boldsymbol{F_d} - V_p \nabla p + m_p \boldsymbol{g} + \boldsymbol{F_c} \tag{4}$$

where m_p is the mass of the particle, $\boldsymbol{u_p}$ is the velocity of the particle, and V_p is the volume of the particle.

On the right-hand side of Eq. (4), the first term $\boldsymbol{F_d}$ is the drag force, which comes from the interaction of the particle and its surrounding fluid. Currently, the computation of the drag force relies on the semi-empirical correlation, which will be presented in detail later. The second term comes from the pressure difference around the sphere; the third term sources from gravity, and the last term $\boldsymbol{F_c}$ is the contact force between the solids (particle-particle or particle-wall). $\boldsymbol{F_c}$ is one of the main differences between the DEM and MPPIC, so it will be discussed separately in the following paragraphs.

2.1.3 Contact force in DEM

For DEM, we choose linear spring-dashpot (LSD) model to calculate the contact force, which treats the particles as a soft, elastic sphere and resolves the collision by calculating a spring-dashpot-slider system. Wang et al. [36] conducted a comprehensive comparison of LSD and non-linear Hertzian collision models when simulating biomass gasification in a fluidized bed. They found the LSD model can tremendously reduce the computational load. Thus, the LSD model is used in the present work. Details about the LSD can refer to [29]. In LSD model, the contact force is the combination of spring

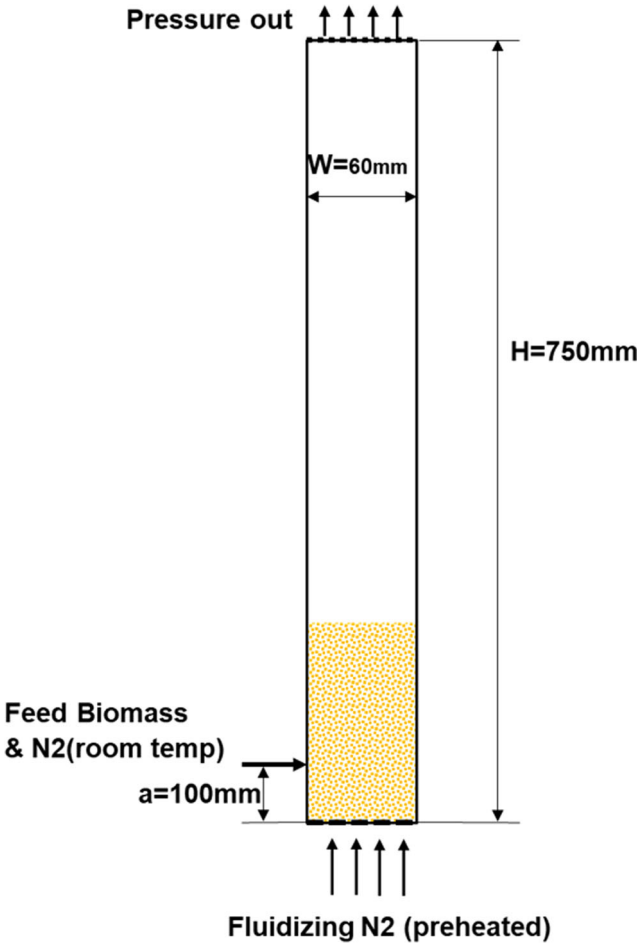

Fig. 1 The geometry of the gasifier

force, damping force, and friction force, which can be decomposed in the normal direction and tangential direction:

$$\boldsymbol{F_c} = \sum_{j=1,j\neq i}^{N}\left(\boldsymbol{F_{ij}^n} + \boldsymbol{F_{ij}^t}\right) \tag{5}$$

Table 2 Boundary condition and initial condition

Boundary condition	
Bottom gas inlet	4.1665e-5kg/s (SBR=1)
	20%wt. H_2O 80%wt. N_2 770°C (1043 K)
Top pressure outlet	1 atm
Biomass inlet	30g/h (8.333e-6kg/s)
Initial condition	
Initial bed height	132.6 mm
Sand density	2640kg/m^3
$\varepsilon_{p,0}$	0.411
ε_{cp}	0.61
Initial temperature	770°C (1043K)
Number of sands	about 7000

Table 3 Proximate analysis and ultimate analysis of the biomass [50]

Name	Rec. basis (wt.%)	Dry basis (wt.%)	DAF basis (wt.%)
Moisture	7.9	-	-
Ash	1.16	1.26	-
Volatiles	72.45	78.66	79.67
Fixed carbon	18.49	20.08	20.33
C element	46.65	50.65	51.3
H element	5.55	6.03	6.1
O element	38.74	42.06	42.6

$$\boldsymbol{F_{ij}^n} = -\left(k_{n,ij}\delta_{n,ij} - \eta_{n,ij}\delta_{n,ij}\right) \tag{6}$$

$$\boldsymbol{F_{ij}^t} = \begin{cases} -\left(k_{t,ij}\delta_{t,ij} - \eta_{t,ij}\delta_{t,ij}\right), & \boldsymbol{F_{ij}^t} \le \mu\left|\boldsymbol{F_{ij}^n}\right| \\ -\mu\left|\boldsymbol{F_{ij}^n}\right|, & \boldsymbol{F_{ij}^t} > \mu\left|\boldsymbol{F_{ij}^n}\right| \end{cases} \tag{7}$$

where $\boldsymbol{F_{ij}^n}$ and $\boldsymbol{F_{ij}^t}$ are respectively the normal and tangential contact force between the colliding particles i and j. The collided particles can be greater than two, so N is given as the number of contacted particles. The $k_{n,ij}$ and $k_{t,ij}$ are the spring stiffnesses in the normal and tangential directions, respectively. The $\delta_{n,ij}$ is the distance of the overlap. The $\eta_{n,ij}$ is the damping coefficient of the dashpot. The μ is the Coulomb friction coefficient.

The momentum exchange term in the gas phase can be derived here by distributing the force on a particle to the cell:

$$I_{gm} = \frac{1}{V_{CV}}\sum_{k=1}^{N_m}\left(F_d - V_p\nabla p\right)^{(k)}K_{CV}^{(k)} \tag{8}$$

where $(F_d - V_p\,\nabla p)$ represents the drag force and pressure gradient force acting on the particles. V_{CV} is the volume of the control volume. Superscripts (k) indicate the cell index. $K_{CV}^{(k)}$ is a distribution function to distribute the drag force to the Eulerian grid. Details can refer to [24, 30, 37].

2.1.4 Contact force in MPPIC

For the MPPIC, the particle contact force is calculated by the solid stress gradient [32].

Table 4 Physical properties of the biomass species

Species	Mass fraction	Density (kg/m^3)	C_P(J/(kg·K)	MW
Carbon	0.1849	1200	Polynomial[a]	12.0
Ash	0.0116	2640	860	60.0
Volatiles	0.7245	470	526	452.5
Moisture	0.079	998	Polynomial[b]	18.0

[a] Cp of the carbon is given by the polynomial relationship of T [34]

Table 5 Particle kinetic parameters

DEM		MPPIC	
ε_{cp}	0.61	ε_{cp}	0.61
Collision force model	LSD **[37]**	**Collision force model**	Harris & Crighton [25]
μ	0.3	P_s	10 Pa
k_n	1000 N/m	ξ	3.0
k_t	1000×(2/7)N/m	ϵ	1×10^{-8}
η_n/η_t	0.5	η	0.85
e	0.9	e	0.9

$$\boldsymbol{F_C} = -\frac{\pi d_p^3}{6\varepsilon_p}\nabla\tau_p \tag{9}$$

where τ_p is the solid stress, which can be drawn as an analogy to fluid stress. It can be calculated by the following formula given by Harris and Crighton [25]:

$$\tau_s = \frac{P_S\varepsilon_s^{\xi}}{\max\left[\left(\varepsilon_{cp}-\varepsilon_p\right),\epsilon\left(1-\varepsilon_p\right)\right]} \tag{10}$$

The P_s, ξ, and ε are parameters controlling the magnitude of the solid stress, and they are closely related to the bed behavior. The P_s has the unit of pressure, and it is proportional to the solid stress. The ξ is the exponent of solid volume fraction; so, when the region becomes denser, the solid stress will exponentially enlarge. The ϵ is a very small value, and it is to prevent the solid stress from becoming infinity at the close pack, so it is called the nonsingularity constant [22]. It is obvious that a larger P_s, larger ξ, and smaller ϵ will produce a larger solid stress, which means more dynamic particles in the fluidized bed. Here we take $P_S = 10$, $\xi = 3$, $\epsilon = 1\times10^{-8}$.

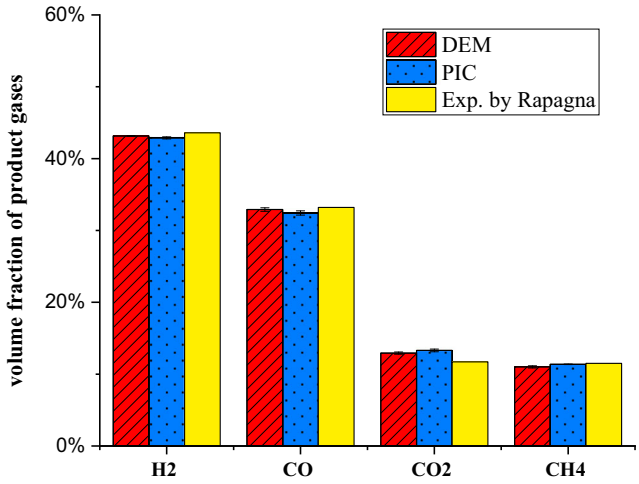

Fig. 2 Model validation by comparing the yields of product gases

In addition, for the MPPIC, the particle distribution function (PDF) f is utilized to calculate the probability of collision. The underlying idea of the PDF is as follows: for a specific particle heading to a specific region, the more other particles gathered in that region, the higher probability this specific particle will collide in that region. The Liouville's equation that involves f can be written as [33, 38]

$$\frac{\partial f}{\partial t} + \nabla\cdot\left(f\boldsymbol{u_p}\right) + \boldsymbol{\nabla u_p}\cdot\left(f\frac{d\boldsymbol{u}_p}{dt}\right) = 0 \tag{11}$$

The volume fraction of particles is correlated with PDF by

$$\varepsilon_p = \iint f\frac{m_p}{\rho_p}dm_p d\boldsymbol{u}_p \tag{12}$$

Usually, Louisville's equation will not be solved directly. Instead, some mathematical manipulation will be adopted. Details can refer to [23].

2.1.5 Drag force

The drag force is given by:

$$\boldsymbol{F_d} = \frac{V_p\beta}{\varepsilon_p}\left(\boldsymbol{u}_f-\boldsymbol{u}_p\right) \tag{13}$$

where β is the interphase momentum exchange coefficient, given by Giadaspow's correlation [39]

$$\beta = \begin{cases} 150\dfrac{\varepsilon_p^2\mu_f}{\varepsilon_f^2 d_p^2} + 1.75\dfrac{\varepsilon_p\rho_f}{\varepsilon_f d_p}\left|\boldsymbol{u}_f-\boldsymbol{u}_p\right| & \varepsilon_f < 0.8 \\ \dfrac{3}{4}C_d\dfrac{\varepsilon_p\rho_f}{d_p}\left|\boldsymbol{u}_f-\boldsymbol{u}_p\right|\varepsilon_f^{-2.65} & \varepsilon_f \geq 0.8 \end{cases} \tag{14}$$

$$C_d = \begin{cases} \dfrac{24}{Re_p}\left(1+0.15\,Re_p^{\,0.687}\right) & Re_p < 1000 \\ 0.44 & Re_p \geq 1000 \end{cases} \tag{15}$$

$$Re_p = \frac{\varepsilon_f\rho_f d_p\left|\boldsymbol{u}_f-\boldsymbol{u}_p\right|}{\mu_f} \tag{16}$$

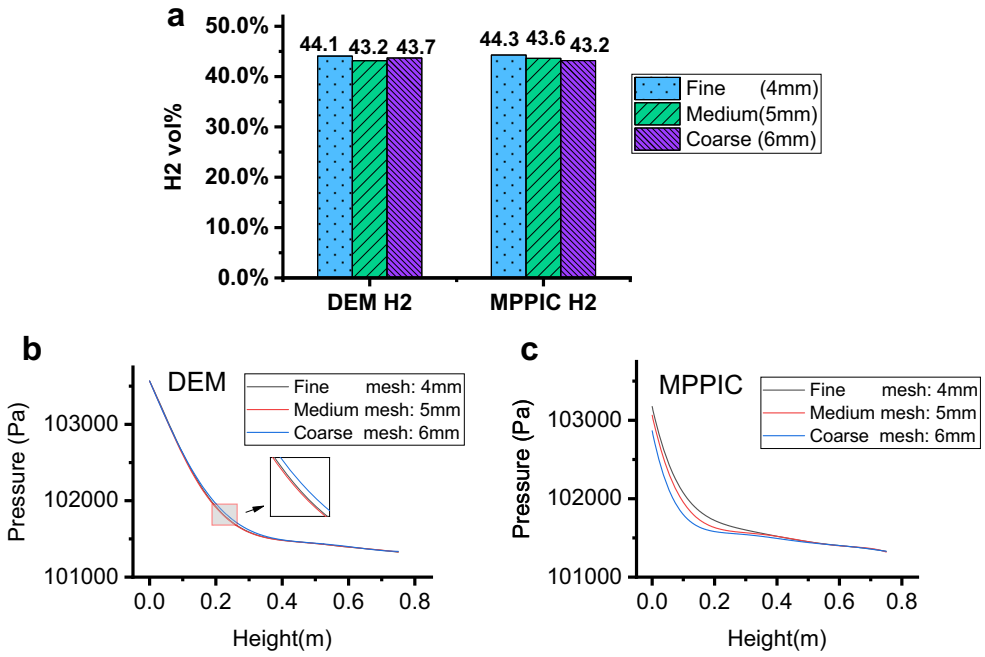

Fig. 3 Grid independence verification of three sets of meshes. (a) Comparison of H_2 volume fractions. (b) Comparison of time-averaged pressure along the centerline against the height, DEM cases. (c) Comparison of time-averaged pressure along the centerline against the height, MPPIC case

2.2 Equations of heat and mass transfer

2.2.1 Gas phase

Mass transfer of fluid phase:

$$\frac{\partial\left(\varepsilon_g\rho_f Y_{f,i}\right)}{\partial t}+\nabla\cdot\left(\varepsilon_g\rho_g Y_f \boldsymbol{u_f}\right)=\nabla\cdot\left(D_i\varepsilon_g Y_{f,i}\right)+\delta\,\dot{m}_{i,chem} \tag{17}$$

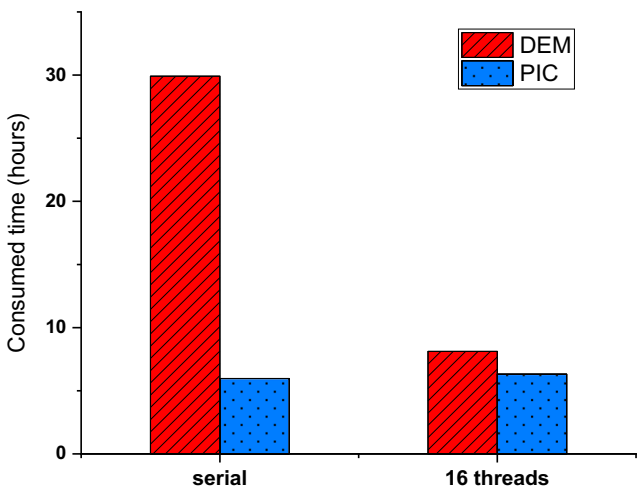

Fig. 4 Comparison of the consumed time

Gas-phase internal energy conservation:

$$\varepsilon_g\rho_g C_{pg}\left(\frac{\partial T_g}{\partial t}+u_{gj}\frac{\partial T_g}{\partial x_j}\right)=-\frac{\partial}{\partial x_i}\left(-k_g\frac{\partial T_g}{\partial x_i}\right)+q_{gs}-\Delta H_{rg}+\gamma_{Rg}\left(T_{Rg}^4-T_g^4\right) \tag{18}$$

The first term on the right-hand side is the heat of conduction; the second term is heat transfer between gas and particle; the third is the heat of reaction; the last term is the gas phase radiative heat transfer, where γ_{Rg} is the gas phase radiative heat transfer coefficient, and T_{Rg} is the gas-phase radiation temperature. Details can refer to [34].

2.2.2 Particle

Conservation of the particle internal energy:

$$m_p C_{p,p}\frac{dT_p}{dt}=\dot{Q}_{pp}+\dot{Q}_{pfp}+\dot{Q}_{pg}+\dot{Q}_{rad}-\Delta H_{rs} \tag{19}$$

where T_p is the particle temperature and $C_{p,\,p}$ is the particle specific heat. On the right-hand side, the $\dot{Q}_{pp}$ is the particle conduction, the $\dot{Q}_{pfp}$ is the particle-fluid-particle conduction, the $\dot{Q}_{pg}$ is the particle-gas convection, the $\dot{Q}_{rad}$ is the radiation, and the ΔH_{rs} is the heat of reactions. Details can refer to [34].

In this work, except for one extra DEM case, the radiation and the conduction are switched off by giving the emissivity and the thermal conductivity as zero, i.e., $\dot{Q}_{pp}=\dot{Q}_{pfp}=\dot{Q}_{rad}=0$. This is to make the DEM and the

Fig. 5 The trajectories (0–1.5 s) of the first entered biomass

MPPIC comparable since it is hard to implement the conduction and radiation in MPPIC cases for now. One extra DEM case is set up to explore the impact of removing the radiation and the conduction. This extra case shows the heat transferred from all five mechanisms. From the result, we can know that conduction and radiation take account for a relatively small portion (about 30%) compared with the convection and the heat of reactions (as is shown later in Section 4.1.4 Fig. 11

In Eq. (19), the particle-particle conduction is given by the Batchelor and O'Brien's model [40]

$$\dot{Q}_{\mathrm{pp}}^{ij} = \frac{4k_p^i k_p^j}{k_p^i + k_p^j}\sqrt{R_p^{k2} - \left(\frac{R_p^{k2} - R_p^{l\,2} + l^{ij2}}{2l^{ij}}\right)^2}\left(T_p^j - T_p^i\right) \tag{20}$$

where k_p is the thermal conductivity. The superscript i and j are the indexes of the contacting particles. The R_p is the radius of the particle. The l^{ij} is the distance between the center of the contacting particles.

The particle-fluid-particle conduction is given by Rong and Horio's model [34, 41]

$$\dot{Q}_{pfp}^{ij} = k_g\left(T_p^j - T_p^i\right)\int_{R_c}^{R_f}\frac{2\pi r}{l^{ij} - \left(\left(R_p^i - r^2\right)^{1/2} + \left(R_p^j - r^2\right)^{1/2}\right)}dr \tag{21}$$

where

$$R_c = \begin{cases} 0 & l^{ij} > 2R_p \\ \sqrt{R_p^{k2} - \left(\frac{R_p^{k2} - R_p^{l\,2} + l^{ij2}}{2l^{ij}}\right)^2} & l^{ij} \le 2R_p \end{cases} \tag{22}$$

$$R_p^k = \max\left\{R_p^i, R_p^j\right\} \tag{23}$$

$$R_p^l = \min\left\{R_p^i, R_p^j\right\} \tag{24}$$

The R_f is the distance delineating the upper bound of the particle-fluid-particle conduction. The R_c is the radius of the circular contact region between two spheres [34].

Particle-gas convection

$$\dot{Q}_{pg} = \gamma_{\mathrm{cp}} A_s\left(T_g - T_p\right) \tag{25}$$

The heat transfer coefficient γ_{pf} is calculated by Ranz-Marshall relation [42]

$$Nu_{fp} = \frac{\gamma_{fp}}{k_g/2R_p} = 2 + 0.6Re^{0.5}Pr^{0.33} \tag{26}$$

The particle-particle radiation is given by

$$\dot{Q}_{rad}^i = \epsilon_{rad} A_s^i \sigma\left(T_{env}^4 - T_i^4\right) \tag{27}$$

where

$$T_{env} = \frac{1}{N_{p,\Omega}}\sum_{j=1, j\neq i}^{N_{p\Omega}} T_p^j \tag{28}$$

ϵ_{rad} is the emissivity. T_{env} is the environmental temperature of the particle, which is the average temperature of the all nearby particles in a region Ω, and the $N_{p,\ \Omega}$ is the number of particles in that region. The detailed illustration can be found in [34].

2.3 Chemical reactions

The reactions considered in this simulation are listed in Table 1. Substances with square brackets represent the concentrations in kmol/m^3. Except for the equations, corresponding reaction rates, IDs, and names are also presented in detail. There are a total of six reactions that simulate three simplified main processes of the lignocellulosic biomass: drying, pyrolysis, and gasification [1, 2, 47–49]. R0 is drying, which is also

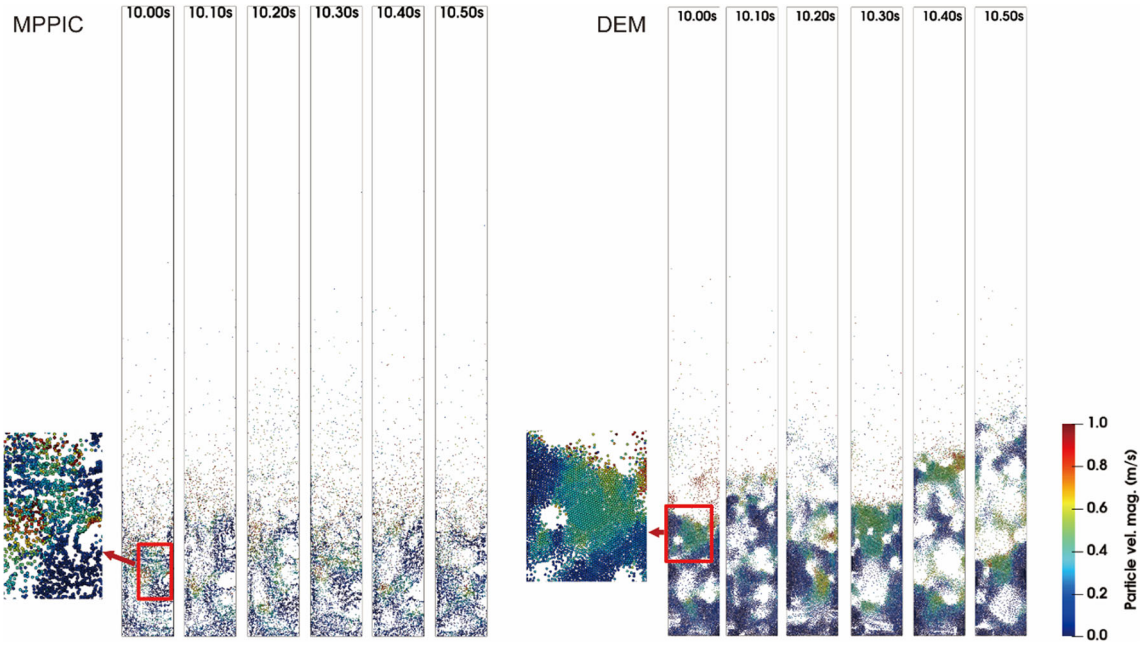

Fig. 6 The particle velocity distribution from 10.0 to 10.5 s

treated as a reaction. R1 is the pyrolysis, which is modeled in a single, lumped reaction. R2 and R3 are heterogeneous reactions. R4 and R5 are homogeneous reactions.

The stoichiometric coefficients of R1 are calculated based on the ultimate analysis and proximate analysis listed in Table 3 [51, 52]. Three assumptions are made during the balancing of the equations: (1) the tar is neglected; (2) the composition of char is considered as carbon; (3) the hydrocarbons are represented by CH_4. These assumptions, along with the simplification of lumped pyrolysis reactions, are also often applied by other researchers [11, 28, 43, 53].

All the reactions consider the chemical reaction kinetics, which calculates the reaction rates based on the first-order Arrhenius formula [54], i.e.,

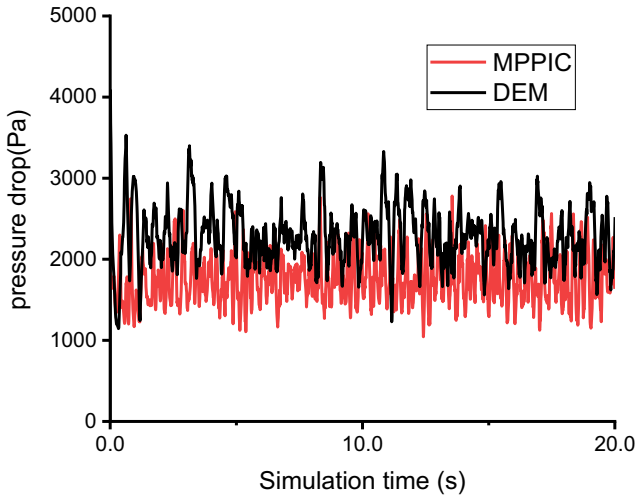

Fig. 7 The evolution of pressure drop

$$k = A \cdot \exp\left(-\frac{E_a}{R_g T}\right) \tag{29}$$

where k is the reaction rate constant. The E_a is the activation energy. A is the pre-exponential factor, $1/s$. R_g is the gas constant of the specific gas, J/(kmol · K). T is the temperature, K. T_p is the particle temperature, and the T_g is fluid temperature, which takes the value of the local cell. The reaction rate will be proportional to the reactant concentration and the reaction rate constant. For instance, for a reaction with two reactants, the reaction rate is

$$r = k[\text{Reacant1}]^a[\text{Reactant2}]^b \tag{30}$$

Except for the reaction kinetic rates, the R2 and R3 also consider the diffusion rate. The r_{kin} represents the kinetic rate, and the r_{diff} represents the diffusion rate. Besides, R5 considers both the forward and the backward reaction, where the r_f represents the forward rate and r_b represents the backward rate.

As for the solid conversion sub-model, the constant density conversion model is used [11, 55].

The diameter of the particle will update after the reactions, and it is calculated by the updated particle mass, i.e.,

$$d_p = \sqrt[3]{\frac{6m_p}{\pi\rho}} \tag{31}$$

The reasons for adopting the constant density conversion model are three: (1) the reaction rates of R2 and R3 (the char conversion reactions) are implemented in the way of surface

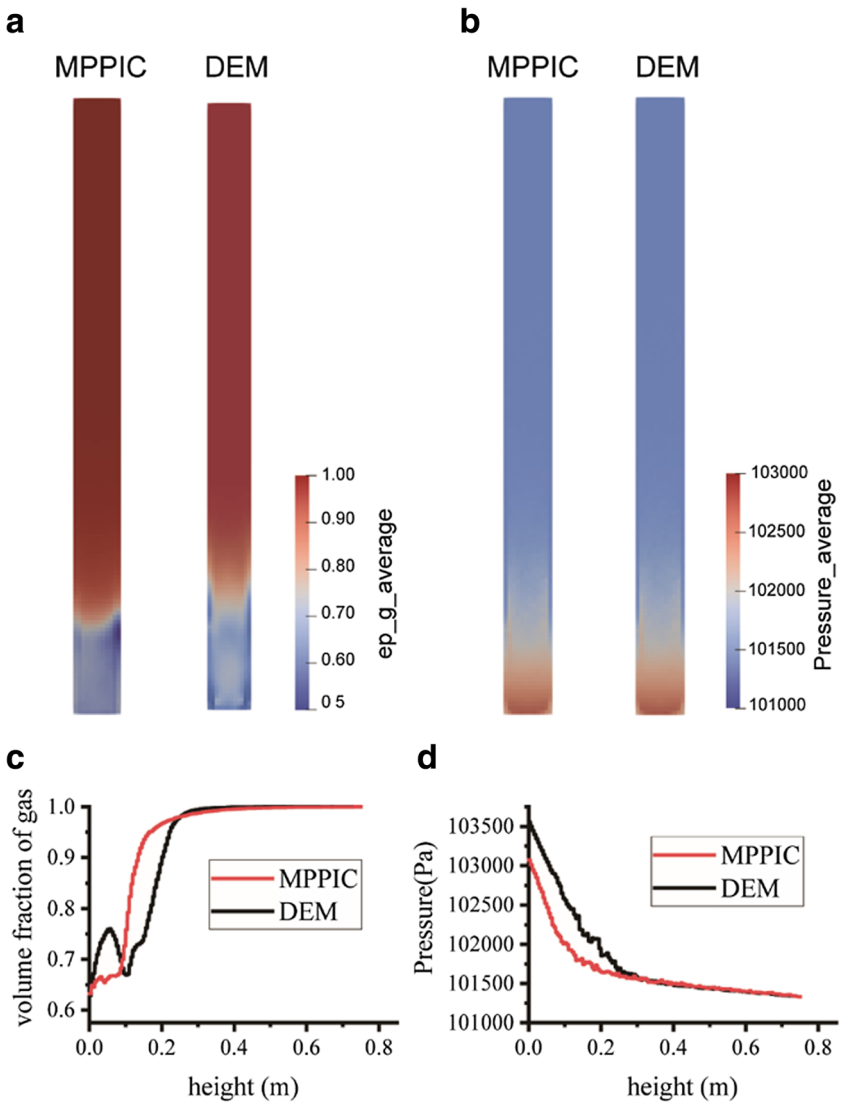

Fig. 8 The time-averaged fields. (a) The contour of time-averaged volume fraction. (b) The contour of time-averaged pressure. (c) The time-averaged volume fraction over the centerline. (d) The time-averaged pressure over the centerline

reactions, which is suitable for the constant density model. (2) More sophisticated models [4] may better depict the intra-particle structure, but they are not as robust as the constant density model. (3) The constant-density conversion model is stable in the simulations with reactions. Other models, for example, the constant-diameter uniform conversion model [4] may easily cause the permanent loss of the reactive particles.

3 Simulation setup

The simulation parameters are set so that it can be compared with the referred experiment of Rapagna [50]. The experiment was conducted in a 60-mm-diameter container, with the steam as the gasifying agent and the almond shell as the feedstock. Further details will be presented in the following paragraphs.

3.1 Geometry and grids

The geometry of the gasifier is shown in Fig. 1. It is a cylinder with fluidizing gas (preheated N_2) blowing up from the bottom, feedstock entering from the side bottom, and product gas releasing out from the top. The height of the container is 750 mm, and the diameter is 60 mm. The lateral feedstock inlet orifice is 100 mm above the bottom.

The grid size is determined to be 5 mm. The total number of grids is 12*150*1=1800. The grid size is limited by the particle size in this study because the unresolved method is used, where the resolved method, e.g., immersed boundary method, is usually unaffordable in computation with more than tens of particles [56]. The unresolved method treats the particles as points with mass and volume. In our simulation, no interpolation algorithm is adopted. Thus, if a particle coincidentally locates at the edge of a cell, the volume and mass will be counted into the cell where the particle center is, and

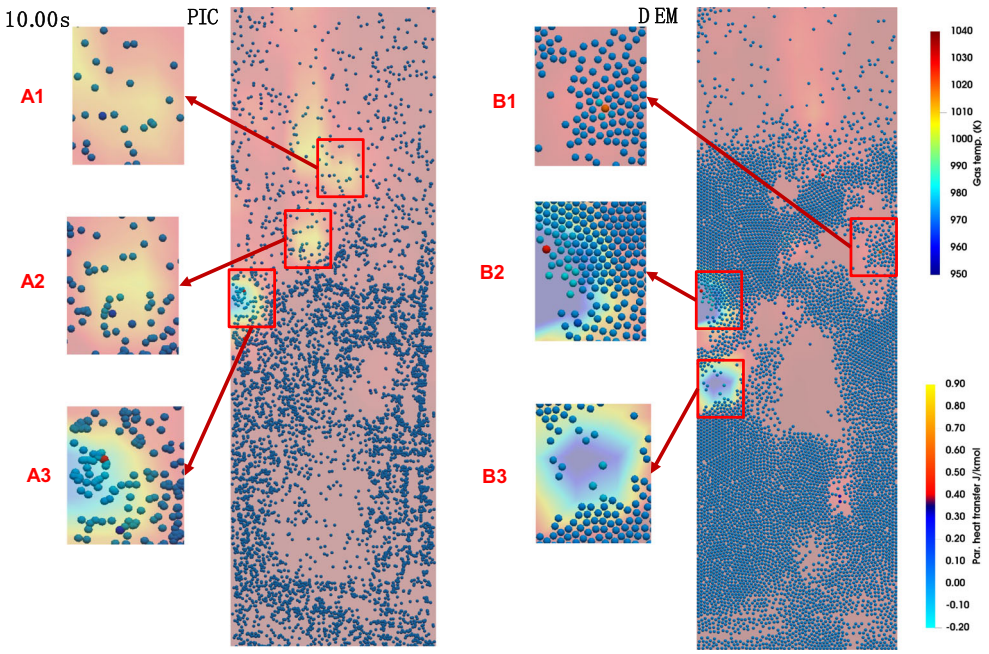

Fig. 9 The distribution of heat transfer on the particles and gas temperature at 10.0 s

thus resulting in the unbalance of the continuity equation [30]. Therefore, to minimize such unbalance, one usual practice is to keep the minimum grid size above 3~5 times [22, 57, 58] of the largest particle diameter [16]. In our simulation, the largest particle size is 1.1 mm; thus, the 5-mm cell is chosen [59].

Besides, a set of quasi-2D grids is adopted to reduce the computation cost. Thus, the third dimension only has one cell and the thickness is the diameter of the largest particle. The quasi-2D is a common practice in fluidized bed simulations [11, 14, 19, 36, 60, 61] since a true 3D computational domain will inevitably increase the particle number to a higher numerical magnitude, but the quasi-2D simulation can successfully simulate the hydrodynamical behavior of the particles [62].

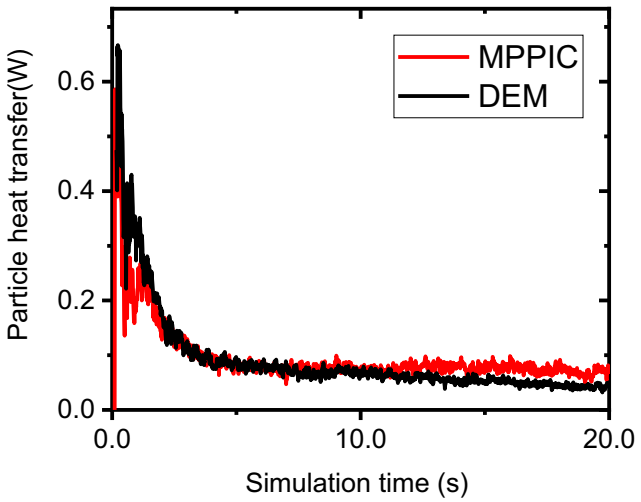

Fig. 10 The evolution of particle heat transfer of the first entered biomass particle

3.2 Boundary condition and initial condition

The boundary condition and the initial condition are listed in Table 2. The fluidizing gas is N_2. The gasifying agent is H_2O, which is mixed with N_2. The steam/biomass ratio (SBR) is 1.

3.3 Physical and chemical properties of biomass

The almond shell is taken as the biomass material, the same as the experiment. Table 3 lists the proximate and ultimate analysis of the biomass [63]. while Table 4 gives the physical properties like Cp and molecular weight of each species in the biomass [50, 64]. The diameter and the density of the biomass particles are given as 1.1 mm and 1200 kg/m^3, respectively. The diameter and the density of sand particles are 1 mm and 2640 kg/m^3, respectively.

$$\frac{C_p}{R_g} = \begin{cases} a_1^L + a_2^L T + a_3^L T^2 + a_4^L T^3 + a_5^L T^4 + a_6^L T^5 + a_7^L T^6, & T \le 1000K \\ a_1^H + a_2^H T + a_3^H T^2 + a_4^H T^3 + a_5^H T^4 + a_6^H T^5 + a_7^H T^6, & T > 1000K \end{cases} \quad (32)$$

The $a_1^L, a_2^L, \ldots, a_7^L, a_1^H, a_2^H, \ldots, a_7^H$ are given from the database of Burcat [64]

The R_g is the gas constant of the specific gas

[b]Cp of the moisture is also given by the polynomial as well, referring to the data from [64]

3.4 Particle kinetic parameters

Table 5 lists the particle kinetic parameters. These parameters are utilized to simulate the movement and the collision of the particles; thus, they directly affect the hydrodynamical

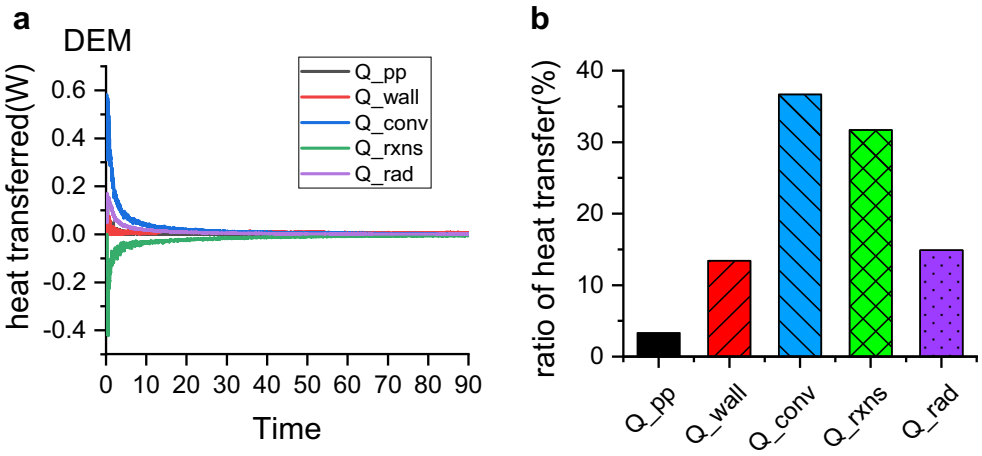

Fig. 11 The heat transfer rates from five different mechanisms: particle-particle conduction (Q_pp), particle-wall conduction (Q_wall), convection (Q_conv), heat of reactions (Q_rxns), and radiation (Q_rad). Note that the Q_pp includes the particle-fluid-particle conduction. (a) The evolution of heat transfer rates. (b) The ratio of heat transfer from five mechanisms by integration (0–90 s)

behavior of the fluidized bed. Efforts are made to minimize the discrepancy of DEM and MPPIC in particle kinetics. The collision force model in DEM is given as linear-spring-dashpot (LSD) model, where $\mu, k_n, k_t, \eta_n/\eta_t, e$ are the parameters controlling the collision force. The P_s, ξ, and ε are parameters controlling the solid stress in MPPIC, as mentioned before. Here we give a common value for it [22, 25].

3.5 Other simulation setup

The total simulation time is given as 20 s. The simulation tool is the open-source multiphase CFD software–MFiX [65, 66], whose codes have been verified robust and effective by many pieces of literature [22, 67]. The initial time step is $1 \times 10^{-4}s$ and the time step varies from $1 \times 10^{-3}s$ to $1 \times 10^{-6}s$ during the simulation. The convergence criterion is given as 1×10^{-3} for continuity and momentum equations, and 1×10^{-4} for energy and species equations. Besides, to strengthen the astringency of chemical reactions stiff chemistry solver is adopted [34].

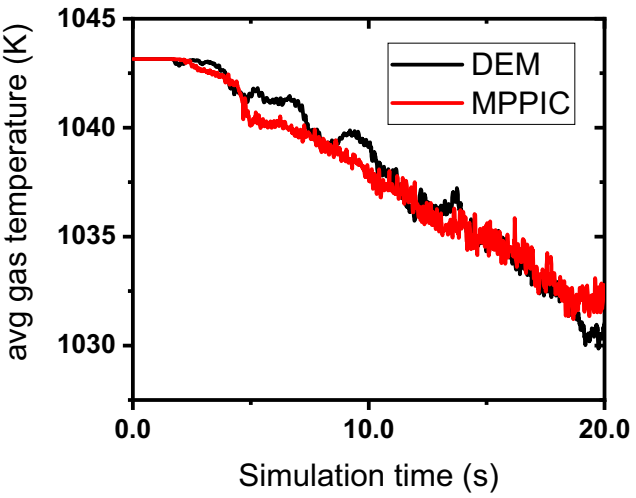

Fig. 12 The evolution of average gas temperature

Additionally, 16-thread DMP (distributed memory parallel) [68] is utilized to accelerate the computation.

4 Results and discussion

4.1 Base case

4.1.1 Model validation

The base case is set up as the previous section described to validate the simulation results. The comparison between the simulations and the experiment in predicting the composition of the product gas is shown in Fig. 2. In this figure, the inert gas N_2 and the steam are removed to make the graph clearer. To eliminate the repetitive error, the base case is repeated three times. The error bar shown in Fig. 2 represents the highest value and lowest value of the three repeated simulations. It can be seen that the difference between the DEM and MPPIC is very small: the difference of H_2 share between the DEM and the MPPIC is 0.26%, and the difference for CO is 0.48%, respectively. In addition, both of them are in accordance with the experiment result: the difference in H_2 share between the experiment and the DEM is 0.45%, and between the experiment and the MPPIC is 0.71%. A similar comparison on CO share is exp. vs. DEM=0.77% and exp. vs. MPPIC=0.29%.

Besides, the repetitive error is calculated as the maximum absolute difference between the simulations and the average value, i.e.,

$$err = \max\left(Vol\%^{H_2}_{sim1,sim2,\ sim3} - Vol\%^{H_2}_{avg}\right)$$

After running three simulations at different dates, the repetitive error is calculated as H_2: 0.57%, CH4: 0.47%, CO: 0.2%, CO_2: 0.22% for the MPPIC cases, and H_2: 0.11%, CH4: 0.10%, CO: 0.03%, CO_2:0.03% for the MPPIC cases.

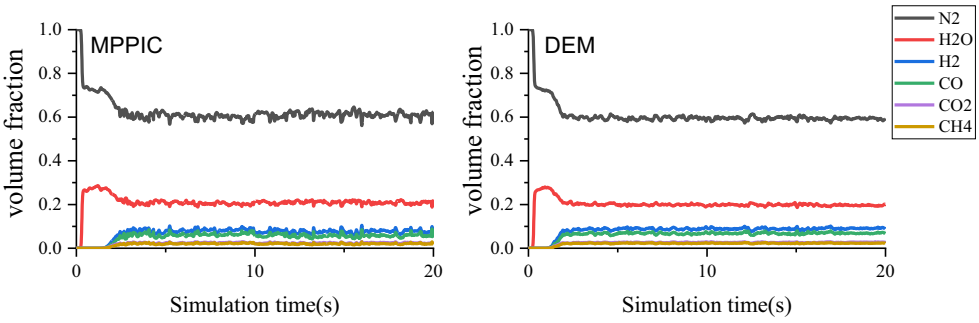

Fig. 13 The evolution of the volume fractions of all 6 gases

The repetitive error gives us a rough estimation of the accuracy can achieve. For instance, all errors smaller than 0.57% for H_2 in MPPIC can be viewed as "accurate" because all errors smaller than the repetitive error are meaningless in numbers.

Again, from the repetitive errors, it can be seen that DEM is more accurate than the MPPIC, but this inaccuracy for the MPPIC is not very serious considering that many factors, like the physical properties and reaction parameters, could contribute to the inaccuracy composition of production gas as well.

4.1.2 Grid independence verification

To prove grid independent, three sets of meshes are compared: coarse mesh (6 mm), medium mesh (5 mm), and fine mesh (4 mm). The result of comparison is shown in Fig. 3; both the differences in H2 vol% and difference in pressure are small, which reveals that all three sets of meshes are usable. Therefore, that we choose the grid size as 5 mm is applicable and reasonable.

4.1.3 Comparison of the consumed time

Two sets of simulations are conducted to find out the difference of consumed time of DEM and MPPIC simulations (as Fig. 4 shows). One is the serial run; the other utilizes 16-thread DMP (distributed memory parallel) with OpenMPI [68]. The result (Fig. 4) shows that in the serial case, the MPPIC will save 23.95 h (80% of the DEM) compared with the DEM, while in the parallel case, the MPPIC only saves 1.8 h (22% of the DEM) compared with DEM. In other words, the MPPIC is roughly five times faster than the DEM in the serial run. Besides, it should be noticed that the parallel running does not save any time for the MPPIC, which is probably because the calculation of the thermo-chemical computation takes up the majority of the time in MPPIC; thus, there is little help to parallelize the job. However, in the DEM case, the parallelization accelerates the job around 3.7 times than the serial run, which is likely because the hydrodynamical computation accounts for a large portion of the consumed time.

4.1.4 Comparison of DEM and MPPIC in the base case

This section focuses on the comparison of DEM and MPPIC results in detail. First, the comparison in hydrodynamics will be implemented. Then, the thermodynamical details will be compared. Finally, the chemical reaction–related parts will be discussed.

Figures 5, 6, and 7 show the particle distributions and particle behaviors.

Figure 5 shows the trajectories of the first entered biomass particle from 0 to 1.5 s. In comparison, the trajectory in the DEM is smoother than the trajectory in the MPPIC, which may be due to the different treatment in the contact force: the DEM has a gradual process of particles overlapping, particles deforming, and the force exerting [24], whereas in the MPPIC it will suddenly exert a solid stress force on the particles when it is judged that the collision happens [25], and thus causing the zigzags of the trajectory.

Figure 6 demonstrates the particle distribution. A zoomed view at 10.0 s is presented as well, from where it can be seen that in the DEM, particles are neatly arranged; however, in the MPPIC, the particles are overlapped and in disorder. Figure 6 also shows the gradual change of the bed from 10.0 to 10.5 s, with an interval of 0.1 s. The particles are colored by the velocity magnitude in the range from 0 m/s to 1 m/s. It can

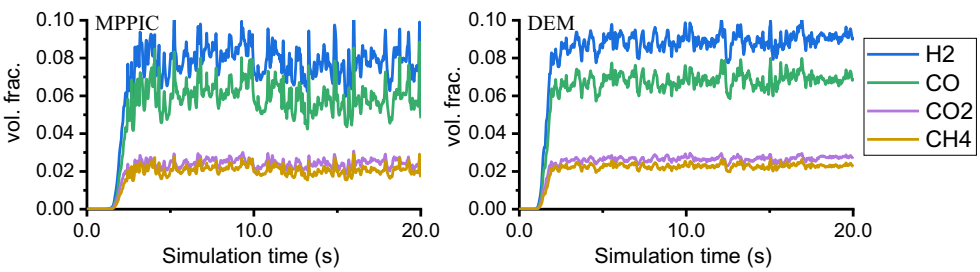

Fig. 14 The evolution of the volume fractions of H_2, CO, CO_2, and CH_4

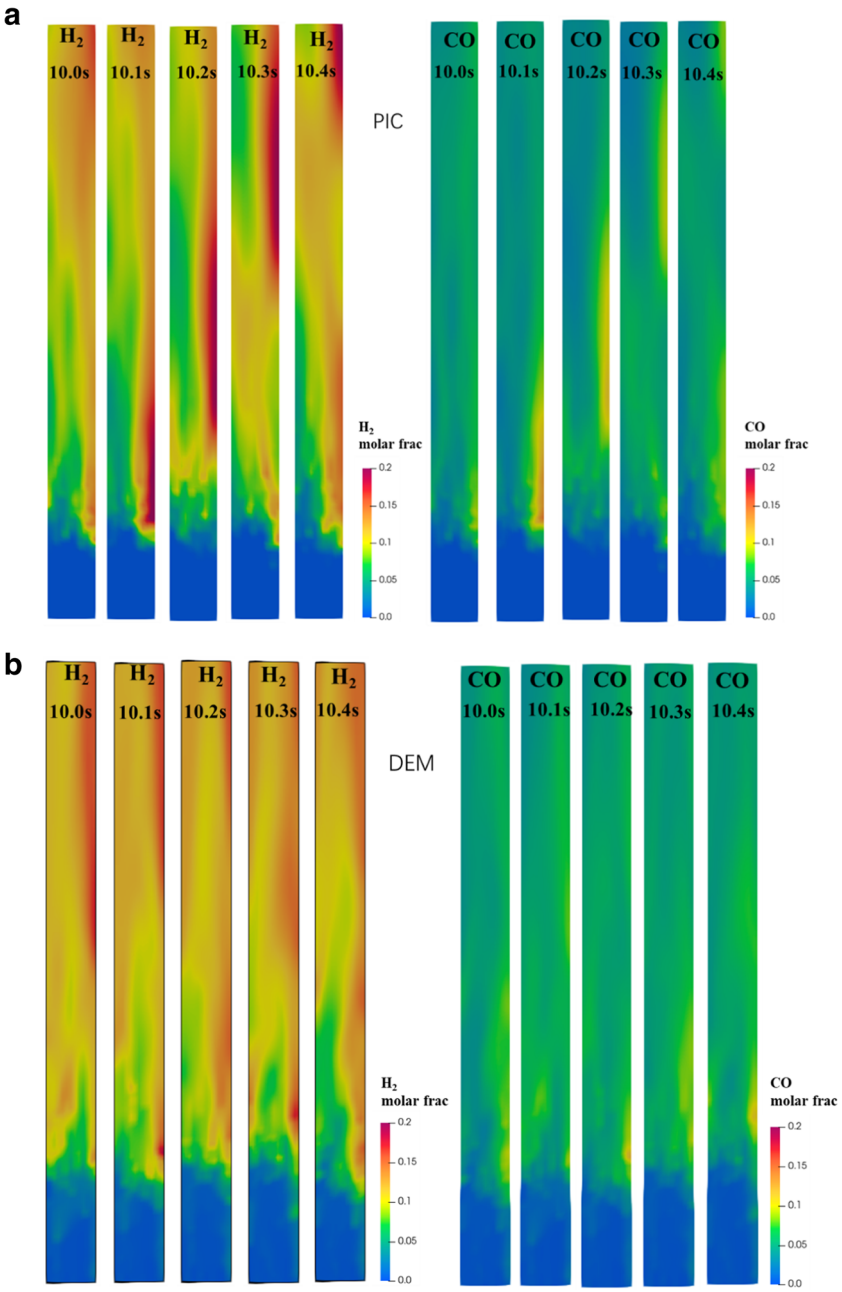

Fig. 15 The molar fraction contour of H_2 and CO. (a) MPPIC H_2 and CO molar fraction contour. From left: time=10.0 s, 10.1 s, 10.2 s, 10.3 s, 10.4 s. (b) DEM H_2 and CO molar fraction contour. From left: time=10.0 s, 10.1 s, 10.2 s, 10.3 s, 10.4 s

be found that the bubble boundaries are clearer in the DEM than in the MPPIC.

Figure 7 shows the evolution of pressure drop. The pressure drop refers to the pressure of the bottom row of cells minus the pressure of the top row of cells. It can be observed that the pressure drop will fluctuate but later becomes quasi-stable, and the trends of MPPIC and DEM are consistent.

Figure 8 shows the time-averaged fields of volume fraction and pressure. The pressure and volume fraction over the centerline of the reactor are drawn as well. The time-averaged pressure drops over the reactor are calculated as 2226 Pa (DEM) and 1741 Pa (MPPIC). The MPPIC and DEM can be compared, and it reveals that the hydrodynamics of the reactor of the two methods are macroscopically similar.

Figures 9, 10, 11, and 12 focus on the thermodynamic details of the fluidized bed.

Figure 9 shows the heat transfer on the particles and the gas temperature. More specifically, the heat transfer rates of particles are shown in different colors. This value is the sum of the right-hand side terms of Eq. (19). Some biomass particles show high heat transfer rate compared with others, which means they are absorbing energy from the surrounding envirnment. Those particles are often in the region of relatively low gas temperatures because the gas will provide the heat.

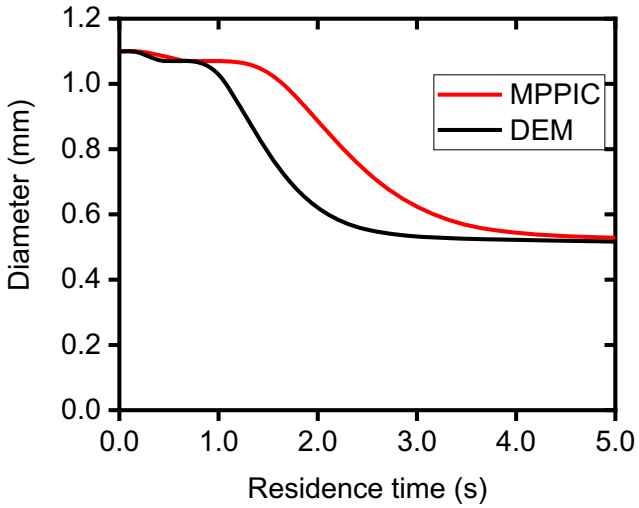

Fig. 16 The evolution of diameter of a selected biomass particle

Figure 10 gives the evolution of the heat transfer rate of the first entered biomass particle. From this figure, it can be seen that the MPPIC and DEM results are in a similar trend. This line chart further explained why the prediction of gases composition of MPPIC and DEM in Fig. 2 is so close: DEM and MPPIC have the totally same parameters concerning reactions (i.e., the stoichiometric coefficients, the formulas of reaction rates, etc.), so the reaction rates are mainly affected by the heat transfer of particles; therefore, when the heat transfer of MPPIC and DEM are similar, the reaction rates will be similar.

In Fig. 11, the detailed five heat-transfer mechanisms in DEM have been discovered. One extra 90-s DEM case is set up to show the long-term evolution of the heat transfer. Figure 11 (a) shows the evolution of heat transfer rates from the five mechanisms: particle-particle conduction (Q_pp), particle-wall conduction (Q_wall), convection (Q_conv), heat of reactions (Q_rxns), radiation (Q_rad). All heat-transfer ways finally converge at zero because we thought the particle and its surroundings (including the gas and neighbor particles) come to the equality of temperatures eventually, while Fig. 12 (b) compares the integration of these five sources. It shows that the Q_conv and the Q_rxns account for over 70% of all heat transfer.

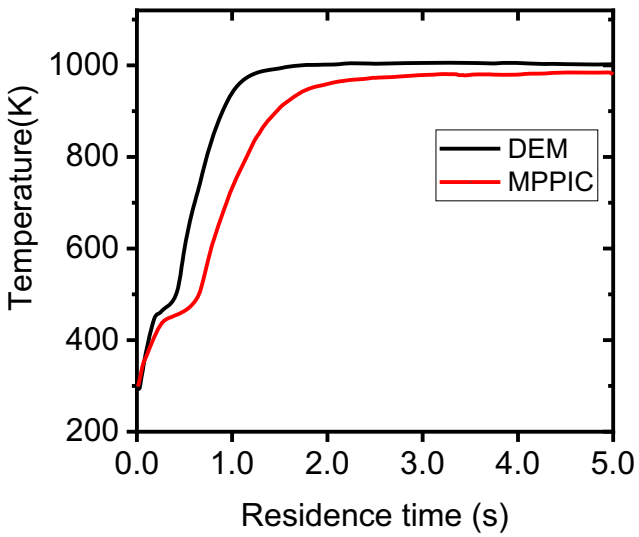

Fig. 17 The evolution of temperature of a selected biomass particle

Remember that the conduction and radiation are not included in MPPIC for now, so this extra case is set up to explore how much impact the radiation and conduction have on the heat transfer, while the result in Fig. 11 tells us that roughly less than 30% of the heat is transferred by conduction and radiation. Note that to make the comparison reasonable, in our other cases the conduction and radiation are switched off.

Figure 12 shows the evolution of the average gas temperature. It can be seen that the temperature declines with fluctuation. This may be because the gasification reactions are endothermic in general.

The discussion concerning chemical reactions will be divided into two parts. First, we will focus on the gas in the reactor; second, the details about the particles will be discussed.

Figures 13, 14, and 15 focus on the product gases species.

Figure 13 shows the evolution of the volume fractions of all 6 gases (H_2O, N_2, H_2, CH_4, CO, CO_2). As shown in Fig. 14, in the beginning, the N_2 takes up 100%. After injecting H_2O, the portion of N_2 drops and the portion of H_2O increases. Then in about 3–4 s, the production of H_2, CO, CH_4, and CO_2 begins. After a while, a quasi-stable stage is observed.

Figure 14 can further corroborate the explanation described in the above paragraphs. In this graph, the steam and nitrogen are removed to make the graph clearer. What can be clearly seen in this chart is the comparison of the relative yields of H_2, CO, CH_4, and CO_2: H_2 ranks first; the next is CO; CO_2 ranks 3rd and the CH_4 is the least.

Figure 15 demonstrates the contour of the H_2 molar fraction and the CO molar fraction from 10.0 to 10.4 s of the MPPIC and of the DEM, respectively. By comparison, a similar distribution of gases can be seen for the DEM and the MPPIC. What is more, one interesting phenomenon is observed: the dense region of the product gases (CO or H_2) will always appear near the right wall surface, which is coincidentally at the height of feedstock inlet orifice, then rise up along the surface until getting out from the top. Why the highest concentrations of product gases initially appear in this spot? One probable explanation is as follows: After the raw biomasses are injected for a small period, right when the biomasses move to the right wall surface facing the orifice ("the spot"), the particles are heated up to an adequate temperature to react. Therefore, this spot has both a high concentration of raw biomasses and a high temperature of particles. That is why the phenomenon happens.

Figures 16, 17, 18, and 19 focus on the evolution of the details of the discrete particles.

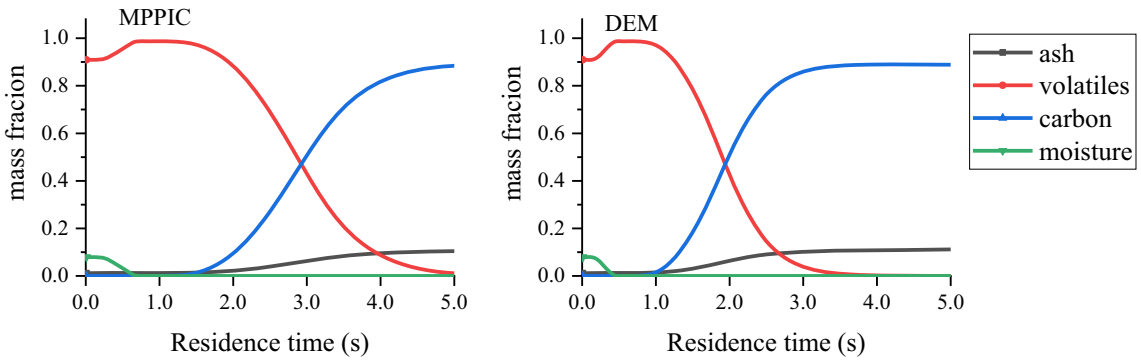

Fig. 18 The evolution of solid species mass fraction of a selected biomass particle

Figure 16 shows the evolution of diameter of a selected biomass particle. In the figure, the diameter of the particle goes down in the beginning, then encounters a small flat zone, and falls again until becomes flat. In the end, the diameter will become roughly the half of the beginning.

Figure 17 depicts the evolution of the temperature of the selected biomass particle in 5 s. From this figure, it can be inferred that the fresh particle will be heated up rapidly from the room temperature (298 K) to bed temperature (1043 K) in about 3 s.

Figure 18 depicts the evolution of the four solid components of the biomass particle: fixed carbon, ash, volatiles, and moisture. The whole process from biomass particles entering to the end of simulation can be divided into three stages: first, 0–1 s, the moisture evaporates at a high reaction rate; thus, at this period, the mass fractions of all other components (including the volatiles) will increase. Then, 1–5 s, the devolatilization dominates the reactions, and the mass fraction of volatiles will drastically decrease, and the share of other species, especially fixed carbon, will rapidly increase. In the last stage, all reactions slow down, and fixed carbon takes up most of the share, with a small but increasing share of the unreacted ash. Although fixed carbon continuously reacts with gases, the reactions in this process are relatively slow compared with the first two stages because they are heterogeneous reactions.

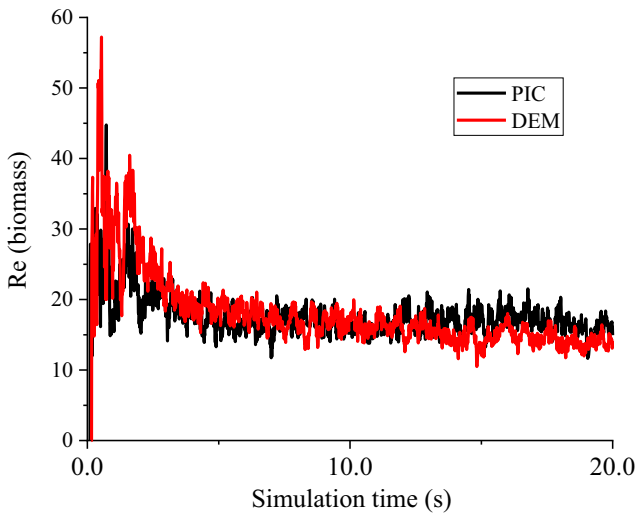

Fig. 19 The evolutions of average Reynolds number of all biomass particles

Figure 19 shows the evolution of the average Reynolds number of all biomass particles. The characteristic velocity is the slip velocity between the particles and the gas, and the characteristic length is the diameter of the particles. It clearly shows that the average Re will be around 20 after the simulation becomes pseudo-stable. The Re is a representation of the movement of particles. Therefore, this graph tells us that the DEM and MPPIC have a discrepancy in the particle movement, but this discrepancy is not large after being averaged.

4.2 Sensitivity analysis

This section will focus on the operating parameters which may affect the gasification result. The volume fractions of H_2 and CO serve as the evaluation indices.

4.2.1 Effect of SBR

Figure 20 demonstrates the change of H_2 and CO volume fractions with SBR. Three SBRs are selected: 0.8, 1.0, 1.2. In our implementation, the ratio of H_2O/N_2 is changed and the other parameters remain unchanged. The picture reveals that as the H_2 volume fraction of DEM and MPPIC simultaneously goes up with increased SBR, the CO volume fraction goes down. It suggests that SBR may contribute to a higher H_2/CO ratio in the product. Also, it proves that MPPIC is capable of giving the same trend as DEM when changing the SBR.

4.2.2 Effect of temperature

Figure 21 shows the effect of temperature on gasification. Three temperatures are selected: 720 °C, 770 °C, 820 °C. The temperatures are applied to the initial condition (the initial packed sands and gas) and the boundary condition (the fluidizing gas). From the chart, it can be seen that higher temperatures are good for improving both H_2 and CO share in the

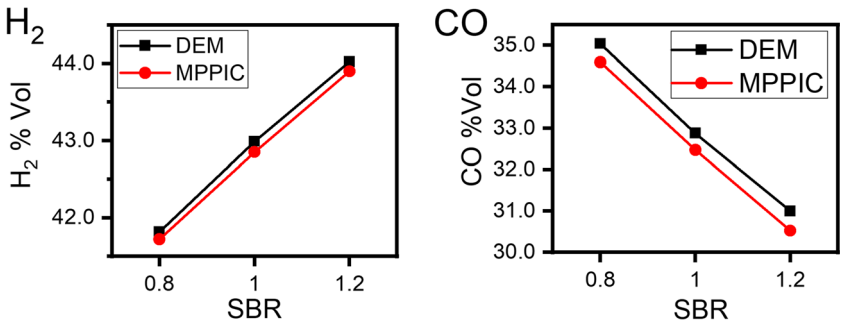

Fig. 20 The change of H_2 and CO volume fractions with SBR

product gas. The trends of DEM and MPPIC cases are consistent as well.

5 Conclusions

This paper sets out to compare the CFD-DEM and MPPIC in simulating the biomass gasification in the fluidized bed. The processes of biomass gasification, including the drying, pyrolysis, heterogeneous reactions, and homogeneous reactions, are simulated and analyzed. The change of the mass fractions of the moisture, ash, fixed carbon and volatiles, and particle diameter with time corroborates the process of gasification. The research has shown that the MPPIC will lose certain accuracy, especially for the particle-scale details, but is roughly five times faster than the DEM. As for the gasification product prediction, the difference of MPPIC and the CFD-DEM is quite small: the prediction of H_2 has an error of 0.45% (DEM) and 0.71% (MPPIC) compared with the experiment, but the difference between the DEM and the MPPIC is as low as 0.26%. The effects of temperature and SBR on the product composition are also explored, and the results also corroborate that the MPPIC and the CFD-DEM will give the same trends when changing these parameters. Therefore, for the particle-scale details, the MPPIC is not as satisfied as DEM because of "overpacking" and other problems; however, if the researcher is expecting a reactor-scale outcome, e.g., the prediction of gas composition, the averaged field quantities, or the effects of operating conditions, the MPPIC is faster and adequately accurate.

NomenclatureGeeks β, Inter-phase momentum exchange coefficient; γ, Heat transfer coefficient; δ_{ij}, Kronecker delta; $\delta_{n,\,ij}$, Normal overlapped distance; $\delta_{t,\,ij}$, Tangential displacement; $\delta\, m_p$, Changing rate of the particle mass; $\delta\, m_{i,chem}$, Changing rate of the gas species i due to chemical reactions; ε, Volume fraction; ε_{cp}, Particle volume fraction of the close-pack; $\varepsilon_{p,\,0}$, Particle volume fraction of the; ϵ, Non-singularity constant; ϵ_{rad}, Radiation emissivity; η, Damping coefficient; λ, Thermal conductivity; μ_g, Viscosity of the gas; μ, Friction coefficient; ξ, Exponential scale factor; ρ, Density; σ, Stefan-Boltzman constant; τ_g, Viscous stress of the gas phase; τ_p, Solid stress of the particle

Symbols CV, Control volume; D_i, Mass transfer coefficient of gas species i; d_p, Diameter of the particle; E_a, Activation energy; e, Restitution coefficient; $\boldsymbol{F_d}$, Drag force; $\boldsymbol{F_c}$, Contact force; f, Particle distribution function (PDF); g, Gravitational acceleration; H, Enthalpy; I_{gm}, Interphase momentum exchange term; K_{CV}, Distribution function to distribute the particle force to the grid; k, Spring stiffness; L, Distance from the particle center to the point of contact; $\boldsymbol{l^{ij}}$, Distance between the centers of the particle i and the particle j; m_p, Particle mass; $\boldsymbol{n_{ij}}$, Vector from the particle i center pointed to particle j center; $\boldsymbol{N_g}$, Number of gas species; P_s, Pressure linear scale factor; p, Pressure; Q, Heat; Re, Reynolds number; r, Radius; Sc, Schmidt number; S_{gij}, Gas-phase stress tensor; T, Temperature; u, Velocity; V_p, Particle volume; Y, Molar fraction

Subscripts cp, Close pack; f, Fluid; g, Gas; p, Particle; i, Particle i or gas species i; $init$, Initial; j, Particle j or gas species j; w, Wall

Superscripts n, Normal direction; t, Tangential direction

Acronyms CFD, Computational fluid dynamics; DEM, Discrete element method; DMP, Distributed memory parallelization; DAF, Dry ash-free; EE, Eulerian-Eulerian method; EL, Eulerian-Lagrangian method; LSD, Linear spring-dashpot; MPPIC, Multiphase particle-in-cell; MW, Molecular weight; SBR, Steam/biomass ratio

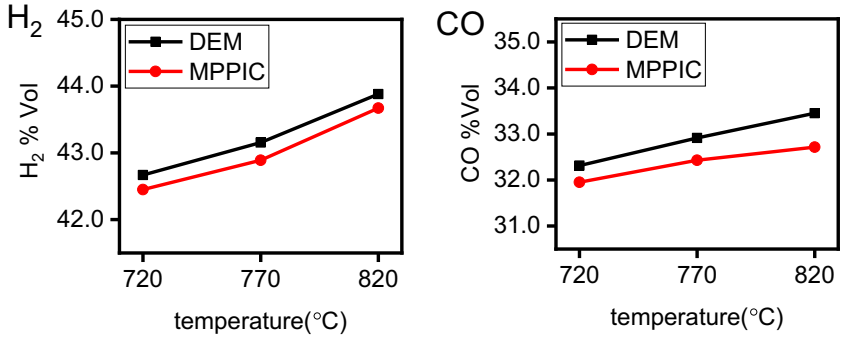

Fig. 21 The change of H_2 and CO volume fractions with temperature

References

1. Sikarwar VS, Zhao M, Clough P, Yao J, Zhong X, Memon MZ, Shah N, Anthony EJ, Fennell PS (2016) An overview of advances in biomass gasification. Energy Environ Sci 9(10):2939–2977. https://doi.org/10.1039/c6ee00935b
2. Kumar A, Jones D, Hanna M (2009) Thermochemical biomass gasification: a review of the current status of the technology. Energies 2(3):556–581. https://doi.org/10.3390/en20300556
3. Ismail TM, Ramos A, Monteiro E, El-Salam MA, Rouboa A (2020) Parametric studies in the gasification agent and fluidization velocity during oxygen-enriched gasification of biomass in a pilot-scale fluidized bed: experimental and numerical assessment. Renew Energy 147:2429–2439. https://doi.org/10.1016/j.renene.2019.10.029
4. Gómez-Barea A, Leckner B (2010) Modeling of biomass gasification in fluidized bed. Prog Energy Combust Sci 36(4):444–509. https://doi.org/10.1016/j.pecs.2009.12.002
5. Zhou ZY, Kuang SB, Chu KW, Yu AB (2010) Discrete particle simulation of particle–fluid flow: model formulations and their applicability. J Fluid Mech 661:482–510. https://doi.org/10.1017/s002211201000306x
6. Chiesa M, Mathiesen V, Melheim JA, Halvorsen B (2005) Numerical simulation of particulate flow by the Eulerian–Lagrangian and the Eulerian–Eulerian approach with application to a fluidized bed. Comput Chem Eng 29(2):291–304. https://doi.org/10.1016/j.compchemeng.2004.09.002
7. Almohammed N, Alobaid F, Breuer M, Epple B (2014) A comparative study on the influence of the gas flow rate on the hydrodynamics of a gas–solid spouted fluidized bed using Euler–Euler and Euler–Lagrange/DEM models. Powder Technol 264:343–364. https://doi.org/10.1016/j.powtec.2014.05.024
8. Moliner C, Marchelli F, Spanachi N, Martinez-Felipe A, Bosio B, Arato E (2019) CFD simulation of a spouted bed: comparison between the discrete element method (DEM) and the two fluid model (TFM). Chemical Engineering Journal 377. https://doi.org/10.1016/j.cej.2018.11.164
9. Ostermeier P, DeYoung S, Vandersickel A, Gleis S, Spliethoff H (2019) Comprehensive investigation and comparison of TFM, DenseDPM and CFD-DEM for dense fluidized beds. Chem Eng Sci 196:291–309. https://doi.org/10.1016/j.ces.2018.11.007
10. Stroh A, Alobaid F, Hasenzahl MT, Hilz J, Ströhle J, Epple B (2016) Comparison of three different CFD methods for dense fluidized beds and validation by a cold flow experiment. Particuology 29:34–47. https://doi.org/10.1016/j.partic.2015.09.010
11. Ku X, Li T, Løvås T (2015) CFD–DEM simulation of biomass gasification with steam in a fluidized bed reactor. Chem Eng Sci 122:270–283. https://doi.org/10.1016/j.ces.2014.08.045
12. Qi T, Lei T, Yan B, Chen G, Li Z, Fatehi H, Wang Z, Bai X-S (2019) Biomass steam gasification in bubbling fluidized bed for higher-H2 syngas: CFD simulation with coarse grain model. Int J Hydrog Energy 44(13):6448–6460. https://doi.org/10.1016/j.ijhydene.2019.01.146
13. Wan Z, Yang S, Sun Y, Wei Y, Hu J, Wang H (2020) Distribution and particle-scale thermochemical property of biomass in the gasifier of a dual fluidized bed Energy Conversion and Management. 209:209. https://doi.org/10.1016/j.enconman.2020.112672
14. Yan L, Lim CJ, Yue G, He B, Grace JR (2016) Simulation of biomass-steam gasification in fluidized bed reactors: model setup, comparisons and preliminary predictions. Bioresour Technol 221:625–635. https://doi.org/10.1016/j.biortech.2016.09.089
15. Wan Z, Yang S, Wei Y, Hu J, Wang H (2020) CFD modeling of the flow dynamics and gasification in the combustor and gasifier of a dual fluidized bed pilot plant. Energy 198. https://doi.org/10.1016/j.energy.2020.117366,
16. Yin W, Wang S, Zhang K, He Y (2020) Numerical investigation of in situ gasification chemical looping combustion of biomass in a fluidized bed reactor. Renew Energy 151:216–225. https://doi.org/10.1016/j.renene.2019.11.016
17. Zhou T, Yang S, Wei Y, Hu J, Wang H (2020) Impact of wide particle size distribution on the gasification performance of biomass in a bubbling fluidized bed gasifier. Renew Energy 148:534–547. https://doi.org/10.1016/j.renene.2019.10.059
18. Zhao L, Lu Y (2018) Hydrogen production by biomass gasification in a supercritical water fluidized bed reactor: a CFD-DEM study. J Supercrit Fluids 131:26–36. https://doi.org/10.1016/j.supflu.2017.07.022
19. Wang S, Luo K, Hu C, Sun L, Fan J (2018) Impact of operating parameters on biomass gasification in a fluidized bed reactor: an Eulerian-Lagrangian approach. Powder Technol 333:304–316. https://doi.org/10.1016/j.powtec.2018.04.027
20. Cundall PA, Strack ODJg (1979) A discrete numerical model for granular assemblies. 29 (1):47-65
21. Andrews MJ, O'Rourke PJ (1996) The multiphase particle-in-cell (MP-PIC) method for dense particulate flows. Int J Multiphase Flow 22(2):379–402
22. Lu L, Gopalan B, Benyahia S (2017) Assessment of different discrete particle methods ability to predict gas-particle flow in a small-scale fluidized bed. Ind Eng Chem Res 56(27):7865–7876. https://doi.org/10.1021/acs.iecr.7b01862
23. Dale MS, Peter JOR (2011) The multiphase particle-in-cell (MP-PIC) method for dense particle flow. In: Sreekanth P, Madhava S, Thomas JOB (eds) Computational gas-solids flows and reacting systems: theory, methods and practice. IGI Global, Hershey, PA, USA, pp 277–314. https://doi.org/10.4018/978-1-61520-651-3.ch009
24. Deen NG, Van Sint AM, Van der Hoef MA, Kuipers JAM (2007) Review of discrete particle modeling of fluidized beds. Chem Eng Sci 62(1-2):28–44. https://doi.org/10.1016/j.ces.2006.08.014
25. Harris SE, Crighton DG (1994) Solitons, solitary waves, and voidage disturbances in gas-fluidized beds. J Fluid Mech 266:243–276. https://doi.org/10.1017/S0022112094000996
26. Hu C, Luo K, Wang S, Sun L, Fan J (2019) Influences of operating parameters on the fluidized bed coal gasification process: a coarse-grained CFD-DEM study. Chem Eng Sci 195:693–706. https://doi.org/10.1016/j.ces.2018.10.015
27. Ostermeier P, Fischer F, Fendt S, DeYoung S, Spliethoff H (2019) Coarse-grained CFD-DEM simulation of biomass gasification in a fluidized bed reactor Fuel 255. https://doi.org/10.1016/j.fuel.2019.115790,
28. Lu L, Benyahia S (2018) Advances in coarse discrete particle methods with industrial applications. In: Bridging scales in modelling and simulation of non-reacting and reacting flows. Part II, Advances in chemical engineering, pp 53–151. https://doi.org/10.1016/bs.ache.2017.12.001
29. Garg R, Galvin-Carney J, Li T, Pannala S (2012) Documentation of open-source MFIX–DEM software for gas-solids flows.
30. Hoomans BPB, Kuipers JAM, Briels WJ, van Swaaij WPM (1996) Discrete particle simulation of bubble and slug formation in a two-dimensional gas-fluidised bed: a hard-sphere approach. Chem Eng Sci 51(1):99–118. https://doi.org/10.1016/0009-2509(95)00271-5
31. Chen X, Wang J (2014) A comparison of two-fluid model, dense discrete particle model and CFD-DEM method for modeling impinging gas–solid flows. Powder Technol 254:94–102. https://doi.org/10.1016/j.powtec.2013.12.056
32. Upadhyay M, Park HC, Choi HS (2018) Multiphase fluid dynamics coupled fast pyrolysis of biomass in a rectangular bubbling fluidized bed reactor: process intensification. Chem Eng Process Process Intensif 128:180–187. https://doi.org/10.1016/j.cep.2018.04.028
33. Snider DM, Clark SM, O'Rourke PJ (2011) Eulerian–Lagrangian method for three-dimensional thermal reacting flow with

application to coal gasifiers. Chem Eng Sci 66(6):1285–1295. https://doi.org/10.1016/j.ces.2010.12.042
34. Musser JMH (2011) Modeling of heat transfer and reactive chemistry for particles in gas-solid flow utilizing continuum-discrete methodology (CDM). West Virginia University, Dissertation
35. Michaelides E, Crowe CT, Schwarzkopf JD (2016) Multiphase flow handbook. CRC Press
36. Wang S, Luo K, Fan J (2020) CFD-DEM coupled with thermochemical sub-models for biomass gasification: validation and sensitivity analysis Chemical Engineering Science 217. https://doi.org/10.1016/j.ces.2020.115550
37. Zhu HP, Zhou ZY, Yang RY, Yu AB (2008) Discrete particle simulation of particulate systems: a review of major applications and findings. Chem Eng Sci 63(23):5728–5770. https://doi.org/10.1016/j.ces.2008.08.006
38. Snider DM (2001) An incompressible three-dimensional multiphase particle-in-cell model for dense particle flows. J Comput Phys 170(2):523–549. https://doi.org/10.1006/jcph.2001.6747
39. Gidaspow D (1994) Multiphase flow and fluidization: continuum and kinetic theory descriptions. Academic press
40. Batchelor GK, O'brien R (1977) Thermal or electrical conduction through a granular material. Proc.Math. Phys. Eng 355(1682):313–333
41. Rong D, Horio M (1999) DEM simulation of char combustion in a fluidized bed. In: In: Second International Conference on CFD in the Minerals and Process Industries CSIRO. Melbourne, Australia, pp 65–70
42. Ranz WE, Marshall WR (1952) Evaporation from drops. Chem Eng Prog 48(173):141–146
43. Yin W, Wang S, Zhang K, He Y (2020) Investigation of oxygen-enriched biomass gasification with TFM-DEM hybrid model. Chem Eng Sci:211. https://doi.org/10.1016/j.ces.2019.115293
44. Liu H, Cattolica RJ, Seiser R, Liao C-h (2015) Three-dimensional full-loop simulation of a dual fluidized-bed biomass gasifier. Appl Energy 160:489–501. https://doi.org/10.1016/j.apenergy.2015.09.065
45. Syamlal M, Bissett LA (1992) METC gasifier advanced simulation (MGAS) model. USDOE Morgantown Energy Technology Center, WV (United States)
46. Bustamante F, Enick RM, Killmeyer RP, Howard BH, Ciocco MV (2010) Uncatalyzed and wall-catalyzed forward water–gas shift reaction kinetics. AICHE J 51(5):1440–1454
47. Roddy DJ, Manson-Whitton C (2012) Biomass gasification and pyrolysis. Comprehensive renewable energy, In, pp 133–153. https://doi.org/10.1016/b978-0-08-087872-0.00514-x
48. Alauddin ZABZ, Lahijani P, Mohammadi M, Mohamed AR (2010) Gasification of lignocellulosic biomass in fluidized beds for renewable energy development: a review. Renew Sust Energ Rev 14(9):2852–2862. https://doi.org/10.1016/j.rser.2010.07.026
49. Font Palma C (2013) Modelling of tar formation and evolution for biomass gasification: a review. Appl Energy 111:129–141. https://doi.org/10.1016/j.apenergy.2013.04.082
50. Rapagnà S, Jand N, Kiennemann A, Foscolo PU (2000) Steam-gasification of biomass in a fluidised-bed of olivine particles. Biomass Bioenergy 19(3):187–197. https://doi.org/10.1016/S0961-9534(00)00031-3
51. Eri Q, Wu W, Zhao X (2017) Numerical Investigation of the air-steam biomass gasification process based on thermodynamic equilibrium model. Energies 10(12). https://doi.org/10.3390/en10122163
52. Yin C-Y (2011) Prediction of higher heating values of biomass from proximate and ultimate analyses. Fuel 90(3):1128–1132. https://doi.org/10.1016/j.fuel.2010.11.031
53. Gerber S, Behrendt F, Oevermann M (2010) An Eulerian modeling approach of wood gasification in a bubbling fluidized bed reactor using char as bed material. Fuel 89(10):2903–2917. https://doi.org/10.1016/j.fuel.2010.03.034
54. Jemaa M, Abbassi MA, Guedri K, Omri A, Haddad K, Jeguirim M (2016) Kinetic and characteristic studies on the pyrolysis of vine stems, almond shell and Ziziphus wood using thermo-gravimetric analysis (TGA).
55. Bruchmüller J, van Wachem BGM, Gu S, Luo KH, Brown RC (2012) Modeling the thermochemical degradation of biomass inside a fast pyrolysis fluidized bed reactor. AICHE J 58(10):3030–3042. https://doi.org/10.1002/aic.13705
56. Wongkham J, Wen T, Lu B, Cui L, Xu J, Liu X (2020) Particle-resolved simulation of randomly packed pebble beds with a novel fluid-solid coupling method Fusion Engineering and Design:161. https://doi.org/10.1016/j.fusengdes.2020.111953
57. Lu L, Konan A, Benyahia S (2017) Influence of grid resolution, parcel size and drag models on bubbling fluidized bed simulation. Chem Eng J 326:627–639. https://doi.org/10.1016/j.cej.2017.06.002
58. Sande PC, Ray S (2014) Mesh size effect on CFD simulation of gas-fluidized Geldart A particles. Powder Technol 264:43–53. https://doi.org/10.1016/j.powtec.2014.05.019
59. Eri Q, Peng J, Zhao X (2018) CFD simulation of biomass steam gasification in a fluidized bed based on a multi-composition multi-step kinetic model. Appl Therm Eng 129:1358–1368. https://doi.org/10.1016/j.applthermaleng.2017.10.122
60. Ku X, Li T, Løvås T (2014) Eulerian–Lagrangian simulation of biomass gasification behavior in a high-temperature entrained-flow reactor. Energy Fuel 28(8):5184–5196. https://doi.org/10.1021/ef5010557
61. Ku X, Li T, Løvås T (2013) Influence of drag force correlations on periodic fluidization behavior in Eulerian–Lagrangian simulation of a bubbling fluidized bed. Chem Eng Sci 95:94–106. https://doi.org/10.1016/j.ces.2013.03.038
62. Cardoso J, Silva V, Eusébio D, Brito P, Boloy RM, Tarelho L, Silveira JL (2019) Comparative 2D and 3D analysis on the hydrodynamics behaviour during biomass gasification in a pilot-scale fluidized bed reactor. Renew Energy 131:713–729. https://doi.org/10.1016/j.renene.2018.07.080
63. Septien S, Valin S, Peyrot M, Spindler B, Salvador S (2013) Influence of steam on gasification of millimetric wood particles in a drop tube reactor: experiments and modelling. Fuel 103:1080–1089. https://doi.org/10.1016/j.fuel.2012.09.011
64. Burcat A, Ruscic B (2005) Third millenium ideal gas and condensed phase thermochemical database for combustion (with update from active thermochemical tables). Argonne National Lab.(ANL), Argonne, IL (United States),
65. Syamlal M, Rogers W, O'Brien TJ (1993) MFIX documentation theory guide. ; USDOE Morgantown Energy Technology Center, WV (United States),
66. Group MD (2020) The MFiX 20.1 User Guide
67. Herzog N, Schreiber M, Egbers C, Krautz HJ (2012) A comparative study of different CFD-codes for numerical simulation of gas–solid fluidized bed hydrodynamics. Comput Chem Eng 39:41–46. https://doi.org/10.1016/j.compchemeng.2011.12.002
68. Gabriel E, Fagg GE, Bosilca G, Angskun T, Dongarra JJ, Squyres JM, Sahay V, Kambadur P, Barrett B, Lumsdaine A Open MPI: goals, concept, and design of a next generation MPI implementation. In: European Parallel Virtual Machine/Message Passing Interface Users' Group Meeting, 2004. Springer, pp 97-104